



Impact of Mo/Ni alloying on microstructural modulation and low-temperature toughness of high-strength low-alloy steel

Wei Liu¹ · Hong-li Zhao¹ · Bing-xing Wang¹ · Yong Tian¹

Received: 27 July 2023 / Revised: 31 August 2023 / Accepted: 1 September 2023 / Published online: 24 December 2023
© China Iron and Steel Research Institute Group Co., Ltd. 2023

Abstract

The high-strength low-alloy steel plates with varying Ni/Mo contents were manufactured using the thermos-mechanical control process. The investigation was conducted to explore the effect of Ni/Mo microalloying on microstructure evolution and mechanical properties of the steel. The results revealed that the increase in Ni content from 1 to 2 wt.% reduced the transition temperature of ferrite and the growth range of ferritic grain was narrowed, which promoted grain refinement. The optimized combination of grain size, high-angle grain boundaries (HAGBs), and martensite-austenite (M–A) islands parameter contributed to the excellent impact toughness of S1 steel at $-100\text{ }^{\circ}\text{C}$ (impact absorbed energy of 218.2 J at $-100\text{ }^{\circ}\text{C}$). As the Mo increases from 0 to 2 wt.%, the matrix structure changes from multiphase structure to granular bainite, which increases the average effective grain size to $\sim 4.62\text{ }\mu\text{m}$ and reduces HAGBs proportion to $\sim 36.22\%$. With these changes, the low-temperature impact toughness of S3 steel is weakened. In addition, based on the analysis of the characteristics of crack propagation path, it was found that M–A islands with low content ($\sim 2.21\%$) and small size ($\sim 1.76\text{ }\mu\text{m}$) significantly retarded crack propagation, and the fracture model of M–A islands with different morphologies was further proposed. Furthermore, correlation between behaviour of delamination and toughness was further analysed by observing delamination size and impact energy parameters.

Keywords High-strength low-alloy steel · Microstructural regulation · Ni addition · Mo addition · Crack propagation · Low-temperature toughness

1 Introduction

Recently, high-strength low-alloy (HSLA) steels have achieved extensive application in ship plates, automobiles, bridges, and other domains due to their excellent mechanical properties and low cost [1, 2]. Furthermore, as one of the basic mechanical properties of low-carbon alloy steel, enhancing the low-temperature toughness is of great significance to expand its scope of application [3]. The perpetual pursuit of researchers has been to enhance the low-temperature toughness of HSLA steel while maintaining high strength through composition design or process regulation.

Generally, the mechanical property of steel is usually governed by distinct microstructural [4]. For example, Zhao et al. [5] reported that acicular ferrite was conducive to the improvement of toughness, and fine martensite-austenite (M–A) islands and residual austenite can retard crack propagation. Qi et al. [6] demonstrated that, in comparison to lath martensite, acicular ferrite exhibits an improved effective grain boundary density that facilitates the deflection of cracks and hence promotes impact toughness. Hosseini et al. [7] showed that the residual austenite content, the size of copper precipitates, and dislocation density have significant effects on the mechanical properties of steel. Therefore, it is feasible to enhance the toughness of steel by controlling the microstructure (e.g., equal grain size, phase component content, dislocation distribution, precipitation).

Microalloying combined with thermos-mechanical control process (TMCP) is an effective means to obtain desired microstructure of low-carbon steel [8, 9]. The

✉ Yong Tian
tianyong@ral.neu.edu.cn

¹ State Key Laboratory of Rolling and Automation, Northeastern University, Shenyang 110819, Liaoning, China

commonly used alloying elements are Ni, Mo, Nb and Ti, etc. Among them, Nb/Ti is generally considered to be strong forming elements of precipitates. For instance, Hu et al. [10] studied the influence of Ti on medium Mn steel microstructure and mechanical properties. The results indicated that 3% Ti promotes the refinement of the lamellar structure and the precipitation of carbides. Compared with Nb and Ti elements, the effect of Mo on the properties of steel is complex and controversial. For example, Kong et al. [11] showed that the increase in Mo content promoted the formation of M–A islands and weakened the toughness of steel. On the contrary, Fu et al. [12] believe that the addition of Mo inhibits the coarsening of precipitates, which is conducive to improving the impact energy. In addition, Ni element plays a vital role in improving the toughness of HSLA steel [13]. As an austenite stabilizing element, the content of residual austenite/ferrite/bainite can be adjusted by adding Ni [14]. Simultaneously, Ni can effectively reduce dislocation resistance in metal and promote dislocation crossing slip at low temperatures, thereby increasing the energy dissipation and improving the impact toughness [15]. However, the effect of Ni/Mo alloying on the microstructure and mechanical properties of the core of medium thickness ship plate steel has not been systematically studied. Therefore, it is meaningful to further explore the mechanism of Ni/Mo alloying.

Based on the principle of microalloying, HSLA steel with varying compositions was prepared using the TMCP process with a low compression ratio. A comprehensive investigation was conducted on the influence of chemical composition on both microstructural features and mechanical properties. The influence of Ni/Mo content on the evolution of microstructure, the relationship between M–A islands and low-temperature toughness, and toughening mechanism of delamination cracks were emphatically analyzed.

2 Experimental

2.1 Materials

Experimental steel ingots (~ 100 kg) were prepared with high purity metals of Ni, Mo, and Fe, etc. (purity ≥ 99.99

wt.%), which were melted in a vacuum induction furnace. The billet thickness is 120 mm and its chemical composition is listed in Table 1. The steel plates of different compositions are named as S1, S2 and S3, respectively. Generally, the non-recrystallization temperature (T_{nr}) of the steel can be calculated as follows [16, 17]:

$$T_{nr} = 887 + 446w_C + 890w_{Ti} + 363w_{Al} - 357w_{Si} + 6445w_{Nb} - 644w_{Nb}^{1/2} + 732w_V - 230w_V^{1/2} \quad (1)$$

$$A_{F3} = 862 - 182w_C - 76.1w_{Mn} + 1168w_{Ti} + 1121w_S + 1804w_{Nb} - 2852w_N - 0.084w_{Cr} \quad (2)$$

where w_i is the concentration of element i (C, Ti, Al, Si, Nb, V, Mn, S, N, Cr), wt.%. According to Eqs. (1) and (2) and the composition of steel, T_{nr} of S1, S2 and S3 steels is 930.9, 932.3, and 931.9 °C (see Table 1). In addition, T_{nr} is considered to be the highest temperature without recrystallization. To ensure the consistency, S1–S3 steels were subjected to the same TMCP as presented in Fig. 1. Before rolling, the billets were heated to ~ 1200 °C and held for 4 h using a box resistance furnace to guarantee the homogeneity of the microstructure. Then, the $\phi 450$ mm two-high mill, equipped with a water cooling system, was used for two-stage controlled rolling. The hot rolling conditions were as follows: the initial rolling temperature for rough rolling was about 1100–1050 °C, while the finishing rolling temperature was about 820–800 °C. All steel billets were rolled to 32 mm over 7 passes, and the reduction schedule of the 7 passes was: 120 → 100 → 82 → 70 → 61 → 53 → 40 → 32 (mm), while the intermediate billet thickness was 82 mm. After rolling, all the samples were first cooled to ~ 400 °C by water, followed by air cooling to room temperature.

2.2 Mechanical properties testing

Charpy impact tests were executed at temperatures of –20, –40, –60, –80 and –100 °C utilizing an Instron SI-IM Canton MA. The V-notched impact samples were taken along the rolling direction (RD) with dimensions of 10 mm × 10 mm × 55 mm, where the V-notch was positioned along the thickness direction (TD). Tensile tests were conducted at room temperature using a CMT5105-

Table 1 Chemical composition and T_{nr} of HSLA steels

Steel	C/wt.%	Mn/wt.%	Si/wt.%	Ni/wt.%	Cu/wt.%	Nb/wt.%	Ti/wt.%	Mo/wt.%	Fe/wt.%	$T_{nr}/^{\circ}\text{C}$
S1	0.05	1.85	0.206	1.96	0.25	0.03	0.015	–	Balance	930.9
S2	0.05	1.84	0.202	0.97	0.25	0.03	0.015	–	Balance	932.3
S3	0.05	1.85	0.203	0.96	0.25	0.03	0.015	0.20	Balance	931.9

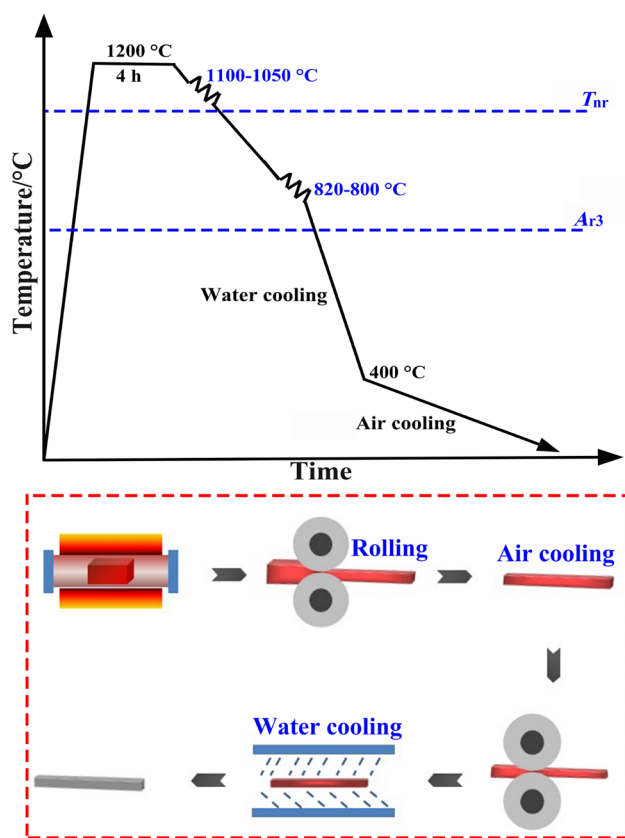


Fig. 1 Processing schematic diagram of rolling and cooling processes of steels

SANS microcomputer-controlled electronic universal testing equipment at a crosshead speed of 3 mm min^{-1} . The V-notched impact samples and tensile samples were obtained from the 1/2 thickness of the steel plates. And every test (impact and tensile test) was performed three times for all samples to guarantee the accuracy of the experimental data.

2.3 Microstructure characterization

The distinctive samples were procured at 1/2 thickness of the steel plate. The standard test samples were mechanically polished and then etched by a 4 vol.% Nital solution. Subsequently, the microstructure was evaluated through the utilization of an optical microscope (OM, Olympus) and scanning electron microscope (SEM, FEI Quanta 600). For transmission electron microscopy (TEM) studies, the samples were mechanically polished from both sides to a final thickness of $\sim 40 \mu\text{m}$. Subsequently, disks with a diameter of 3 mm were punched out and twin-jet polished using 10% perchloric acid in ethanol at $-25 \text{ }^\circ\text{C}$. TEM (FEI, Talos F200X, USA) was operated at 200 keV. Additionally, samples taken after Nital solution etching were treated with LePera solution [18] to better observe the

characteristics of M–A islands by OM. The shape, size, and content of the M–A islands were determined by computer graphics software (Image-Pro Plus, IPP). The fracture morphology of the Charpy impact samples and tensile samples and the crack propagation path of the impact fracture after nickel plating were analyzed via SEM and OM. Moreover, to comprehensively analyze the characteristics of effective grain size (EGS) and grain boundary, etc., an electron back-scattered diffraction (EBSD, ZEISS crossbeam 550) analysis was performed on samples that underwent electropolishing utilizing an electrolyte consisting of 12 vol.% perchloric acid mixed with 88 vol.% ethyl alcohol.

3 Results

3.1 Microstructures

The optical microstructures of S1, S2, and S3 steels at 1/2 thickness are depicted in Fig. 2a, c, e. S1–S3 steels are composed of multiple phases, i.e., polygonal ferrite (PF), acicular ferrite (AF) and granulate bainite (GB), while there exist significant divergences in terms of their content and distribution. S1 steel contained abundant AF ($\sim 45 \text{ vol.}\%$), PF ($\sim 20 \text{ vol.}\%$), and a few GB ($\sim 33 \text{ vol.}\%$). S2 steel contained $\sim 41 \text{ vol.}\%$ AF, $\sim 28 \text{ vol.}\%$ PF and $\sim 26 \text{ vol.}\%$ GB. Compared with S1 and S2 steels, a full GB ($\sim 98 \text{ vol.}\%$) structure has been observed in S3 steel (see Fig. 2e). In addition, SEM images of S1, S2, and S3 steels at 1/2 thickness are depicted in Fig. 2b, d, f. Different shapes of M–A islands were observed in the microstructure of the experimental steels. The granular M–A islands are evenly distributed in grain boundaries and matrix in S1 steel, and a similar situation was observed in S2 steel. In contrast, M–A islands in S3 steel are presented in a disordered distribution with a large size. And some of M–A islands are aggregated into a necklace-like structure, as depicted in Fig. 2f.

In addition, to observe the details of M–A islands in steel, S1–S3 samples were etched again with LePera solution. OM micrographs of M–A islands are illustrated in Fig. 3a, c, e. TEM images are illustrated in Fig. 3b, d, f for S1–S3 steels. M–A islands in S1 and S2 steels tend to appear mostly as fine particles, which transform into large blocks and necklace-like configurations in S3 steel (blue/red line in Fig. 3e, f). It is noteworthy that larger/necklace-like M–A islands tend to form along the grain boundaries, where additional energy and commensurate compositional fluctuations can be obtained (see Fig. 3) [19, 20]. The content and size data of M–A islands collected through IPP are presented in Table 2. Compared to S2 and S3 steels, M–A islands in S1 steel have the smallest size (average size

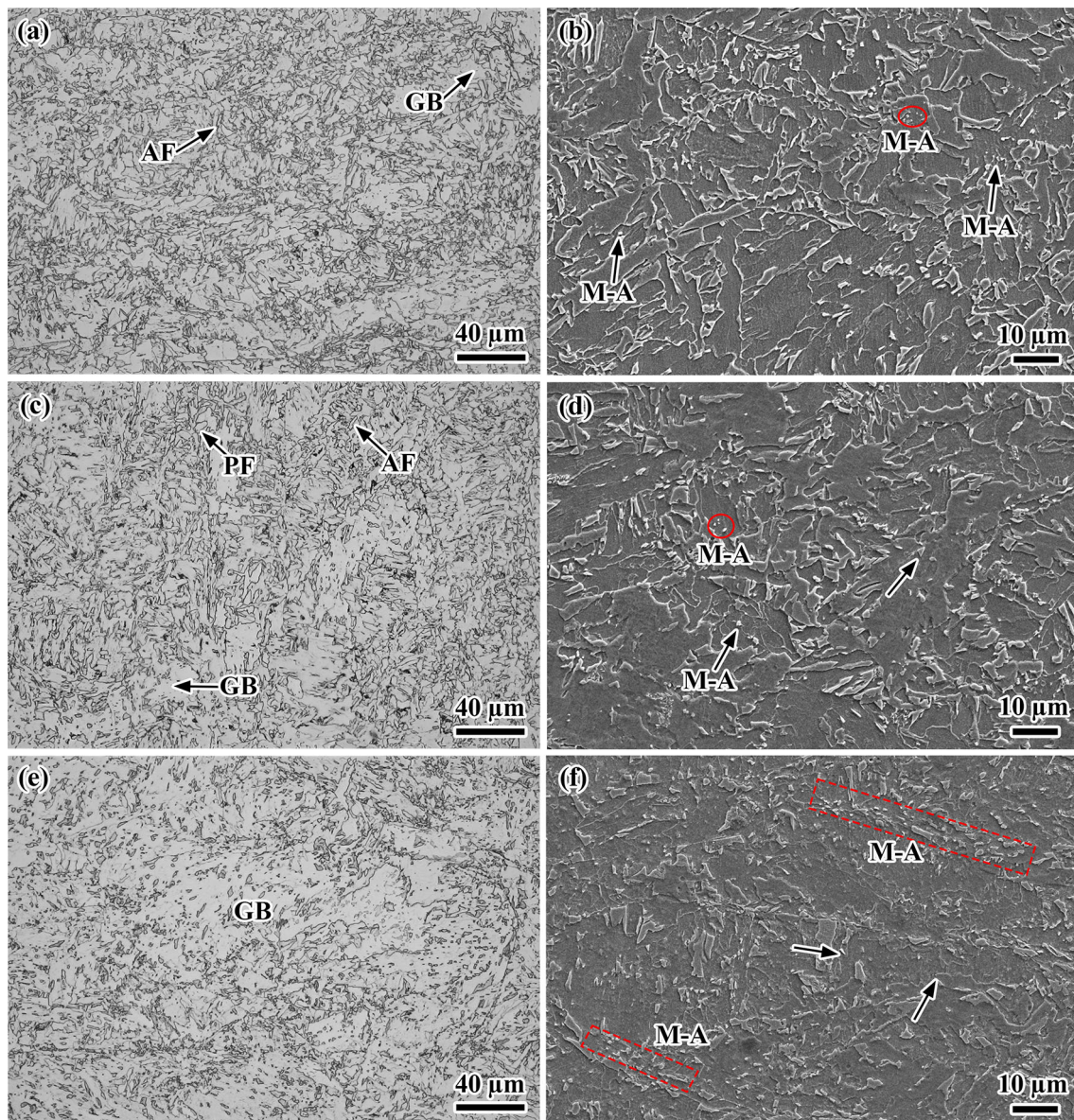


Fig. 2 Microstructure characteristics of S1–S3 steels at 1/2 thickness. **a, b** S1 steel; **c, d** S2 steel; **e, f** S3 steel

of $\sim 1.76 \mu\text{m}$) and the lowest content (2.21%). The difference in M–A islands parameter is intricately linked to the chemical composition, rolling, and subsequent cooling schedules of the steel [21]. Besides, M–A islands could be detrimental to the toughness due to its hard and brittle nature.

Upon conducting further TEM analysis of the steel, spherical carbides have been observed in S1–S3 steels, as depicted in Fig. 4. It can be seen that the carbides are distributed randomly and evenly on the matrix. In addition, the average size of precipitates in S1–S3 steels was further measured. The precipitates in S3 steel are finer ($5.82 \pm 1.3 \text{ nm}$) and more abundant, while the precipitates in S1 ($7.78 \pm 2.6 \text{ nm}$) and S2 ($7.63 \pm 2.4 \text{ nm}$) steels are

coarser and sparser. The energy dispersion spectrum analysis verified that the carbides in S3 steel are predominantly composed of elements like Mo, Nb, and Ti, unlike those in S1 and S2 steels which primarily contain elements like Nb and Ti.

To further analyze crystallographic features and grain boundary characteristics, EBSD characterization was conducted and the inverse pole figure (IPF) maps and grain boundaries distribution maps of the S1–S3 steels at 1/2 thickness are depicted in Fig. 5. The misorientations higher than 15° as high-angle grain boundaries (HAGBs) are represented by blue lines, and the misorientations between 2° and 15° as the low angle grain boundaries (LAGBs) [22] are indicated by the red lines. The grain boundary maps

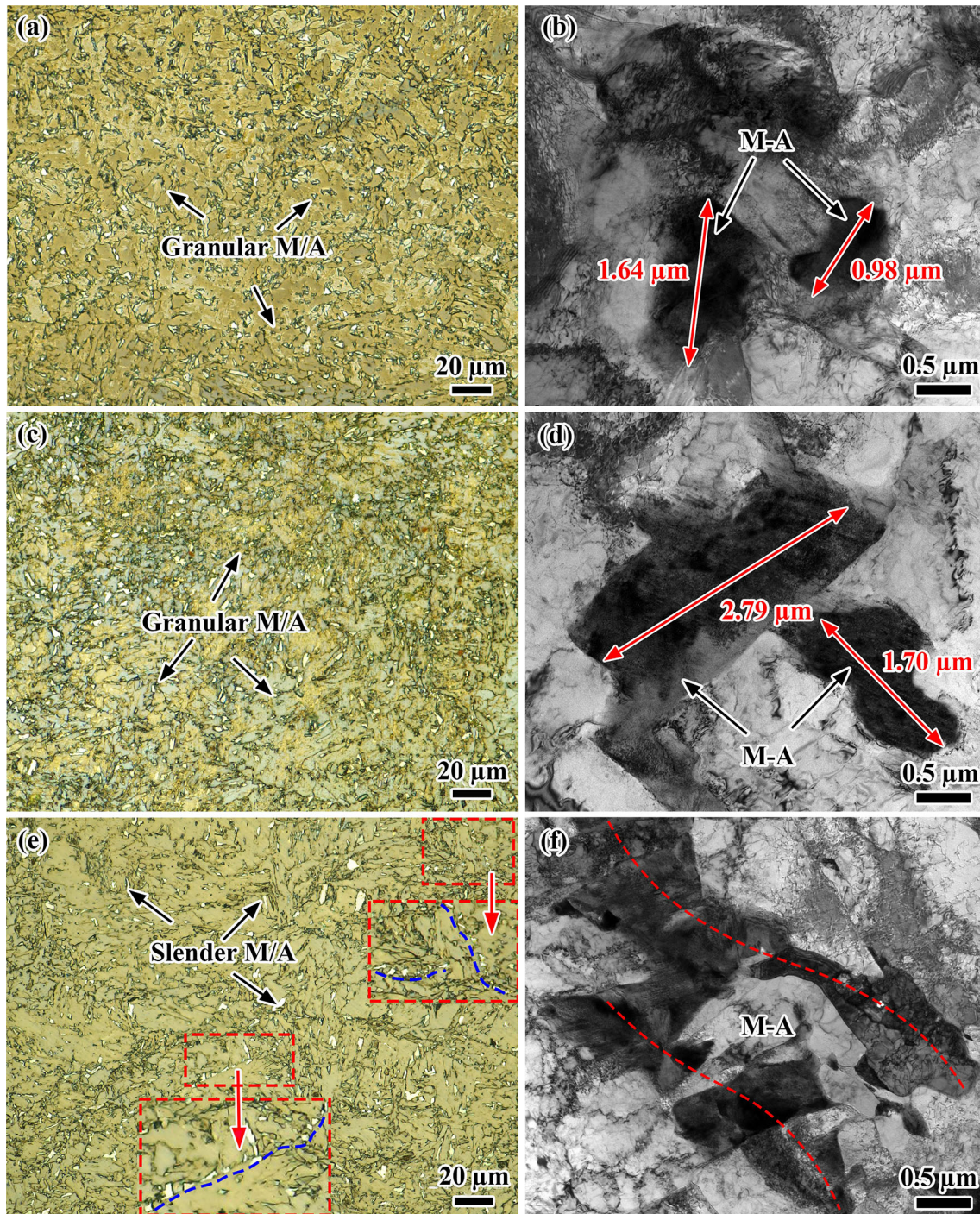


Fig. 3 Morphology and distribution of M/A islands in S1–S3 steels. **a, b** S1 steel; **c, d** S2 steel; **e, f** S3 steel

reveal that the distribution of HAGBs and LAGBs is more uniform in S1 steel than that in S2 and S3 steels (Fig. 5a, c, e). The misorientation angle distribution and fraction of LAGBs and HAGBs are depicted in Fig. 6. The results indicate that HAGBs percentage are evaluated as 43.43%, 47.16%, and 36.22% for S1, S2, and S3 steels, respectively. Additionally, EGS has been further revealed based on the

parameter of HAGBs. Figure 6b presents the average EGS with standard deviation (standard deviation is the arithmetic square root of the variance and reflects the dispersion of a data set). Correspondingly, the average EGS for these samples is 3.60 μm (S1), 3.98 μm (S2), and 4.62 μm (S3), respectively. From the grain boundary misorientation distribution figure maps (Fig. 5a, c, e), it is seen that S1 steel

Table 2 Statistical information of M–A islands at 1/2 thickness obtained by IPP

Sample	Average maximum chord length/ μm	Maximum size/ μm	Content/%
S1	1.76	3.2	2.21
S2	1.88	4.5	2.74
S3	2.80	10.5	3.84

had not only a high proportion of HAGB but also a uniform distribution, which contributed to refining the average EGS.

Considering the above results, it is incontrovertible that the different Ni/Mo contents play a paramount role in determining the microstructure characteristics. The microstructural changes caused by component regulation presumably have an important effect on the properties of the material, so that further delving the mechanical property is necessary.

3.2 Mechanical property

3.2.1 Tensile property

The engineering stress–strain curves and the statistical results of tensile properties of S1–S3 steels at 1/2 thickness are depicted in Fig. 7. S3 and S2 steels had the higher yield and tensile strength, while S1 steel had the superior total elongation. Table 3 shows the detailed tensile data of experimental steels. S1 steel exhibits the lowest tensile strength (667 MPa) at all test temperatures. In contrast, S2 and S3 steels show a higher tensile strength of 689 and 768 MPa, respectively. S1 steel boasts impressive total elongation (25%), whereas the total elongation of S2 and S3 steel falls short at a mere 20% and 17%. Furthermore, the micro-hardness values of S1–S3 steels are recorded as 201.40, 225.50, and 237.15 HV (Fig. 7b), respectively, which corresponds to their tensile properties.

SEM micrographs of the tensile fracture surface are depicted in Fig. 8. Based on the macroscopic fracture diagram, the fracture of all samples exhibited a cup-cone type, accompanied by a prominent necking phenomenon. Moreover, compared with S2 and S3 steels fracture morphology in Fig. 8d, f, it becomes apparent that the dimples on the fracture surface of S1 steel are both larger and deeper. The above-mentioned features indicate that severe plastic deformation occurred in S1 steel during impacting, which is conducive to obtaining more excellent ductility. Furthermore, the plastic deformation energy for dimple formation (U) can be calculated by Eq. (3) [23, 24]:

$$U = \sigma_b \times D_{\text{DP}} \times M \times A_{\text{DP}} \quad (3)$$

where M is constant; D_{DP} is the diameter of the dimple; σ_b is the tensile strength; and A_{DP} is the dimple area. Equation (4) indicates that big and deep dimples are conducive to the enhancement of toughness. Therefore, large diameter dimples ($(D_{\text{S1}} = 6.06 \pm 4.98 \mu\text{m}) > (D_{\text{S2}} = 4.84 \pm 3.45 \mu\text{m}) > (D_{\text{S3}} = 4.63 \pm 2.27 \mu\text{m})$, where D is the average diameter of the dimple on the fracture surface) on the fracture surface can consume more energy, which is conducive to the improvement of ductility.

3.2.2 Charpy impact test and fracture characteristic

The impact energy and fibrous region ratio of S1–S3 steels at 1/2 thickness, tested within the temperature range of -20 to -100 °C, are depicted in Fig. 9. The results show that the impact energy of S1–S3 steels decreases with decreasing test temperature, but the impact energy of S1 steel decreases more slowly than that of S2 and S3 steels, especially at lower temperatures (below -40 °C). S1 steel presents the lowest reduction in impact energy as 91 J at the impact temperature range spanning from -20 to -100 °C. In contrast, S3 steel shows the highest impact energy reduction of 129 J. When the impact temperature is reduced to -100 °C, the impact energy drops to a lower level for S2 (111.4 J) and S3 (18 J) steels. Nevertheless, S1 steel still maintains a higher impact energy (218.2 J), as shown in Fig. 9a.

To conduct a comprehensive observation of the fracture morphology and fracture mode, the fracture morphology of S1–S3 steels tested at -100 °C are performed in Fig. 10. The macroscopic fracture shows that the proportion of fibrous zone on the fracture surface of S1 steel ($\sim 23.3\%$) is significantly higher than that of both S2 ($\sim 7.8\%$) and S3 ($\sim 0\%$) steels (Fig. 9b), indicating that S1 steel presents more excellent impact toughness. In addition, the fracture of S3 steel exhibits typical cleavage facets (Fig. 10h, i), which is a definitive indication of brittle fracture [6, 25]. The relatively flat fracture possessed weak crack propagation restraint, resulting in low impact toughness. Conversely, S1 and S2 steels exhibit complete ductile fractures, which can be distinguishable by a lot of evenly dispersed dimples on the fracture surface (Fig. 10a–f). The large and deep dimples on the fracture surface can effectively absorb substantial energy during the fracture process (which is related to the nucleation and growth of micro-voids), thus retarding the crack initiation and propagation and improving the low temperature toughness [26, 27].

To further analyze the fracture process, the crack propagations path of S1 and S3 steels at -100 °C was performed, as depicted in Fig. 11. The primary crack of S1

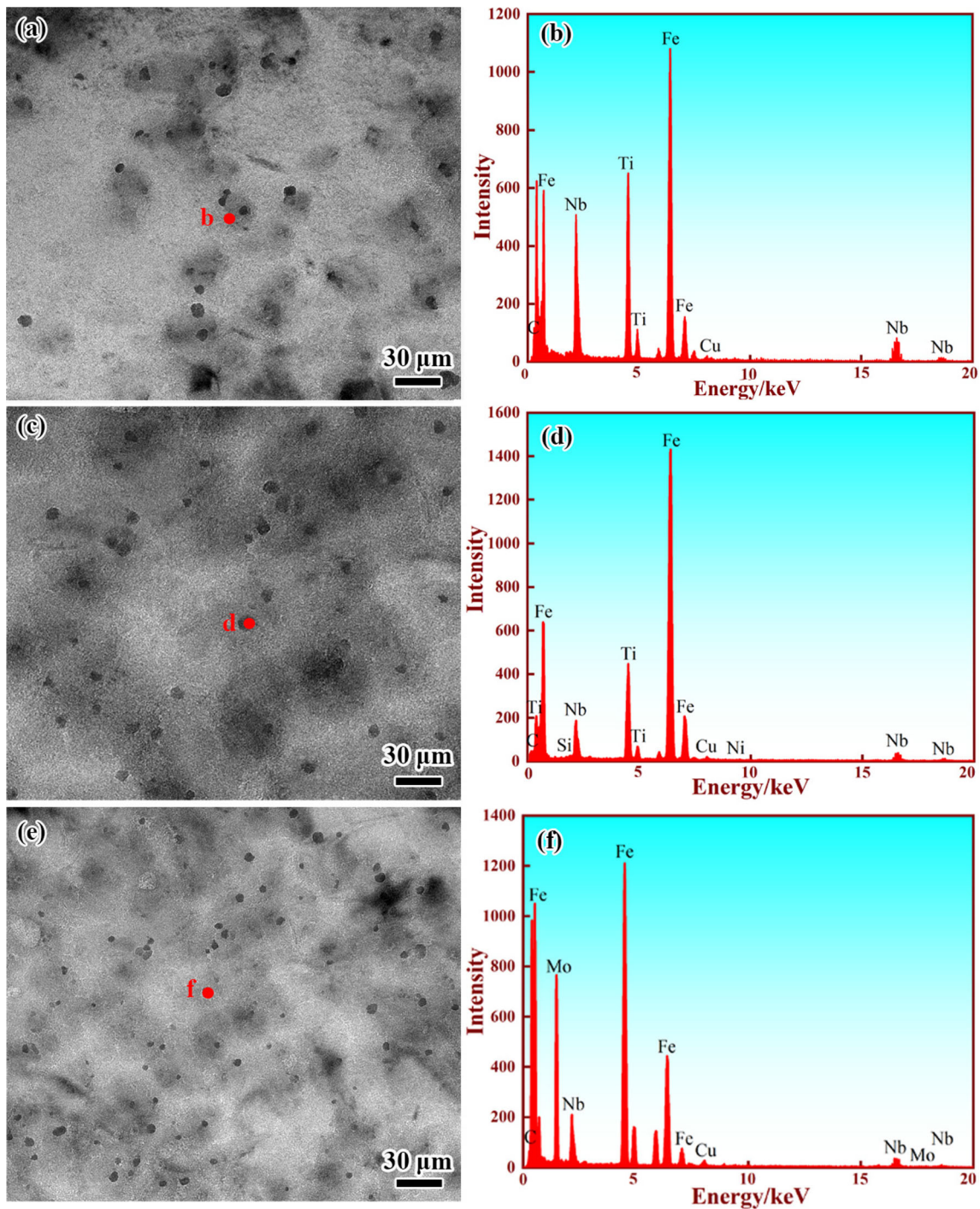


Fig. 4 TEM micrographs (a, c, e) and corresponding TEM-EDX (energy dispersive X-ray spectroscopy) (b, d, f) of nanoprecipitates for S1–S3 steels at 1/2 thicknesses. a, b S1 steel; c, d S2 steel; e, f S3 steel

and S3 steels is propagated in a manner of being straight and deflected alternately. The discrepancy lies that the primary crack of S1 steel shows greater roughness and denser zigzag turning areas (Fig. 11) during the propagation, whereas the primary crack in S3 steel remains comparatively flat, as depicted in Fig. 11. The larger-angle

deflection and more frequent crack deflection will consume more energy, so that the impact toughness of S1 steel is better under the same test conditions. Furthermore, as illustrated in Fig. 11b, c, there are numerous secondary cracks and plastic deformation regions around the large-angle/stable deformation zone in S1 steel. However, S3

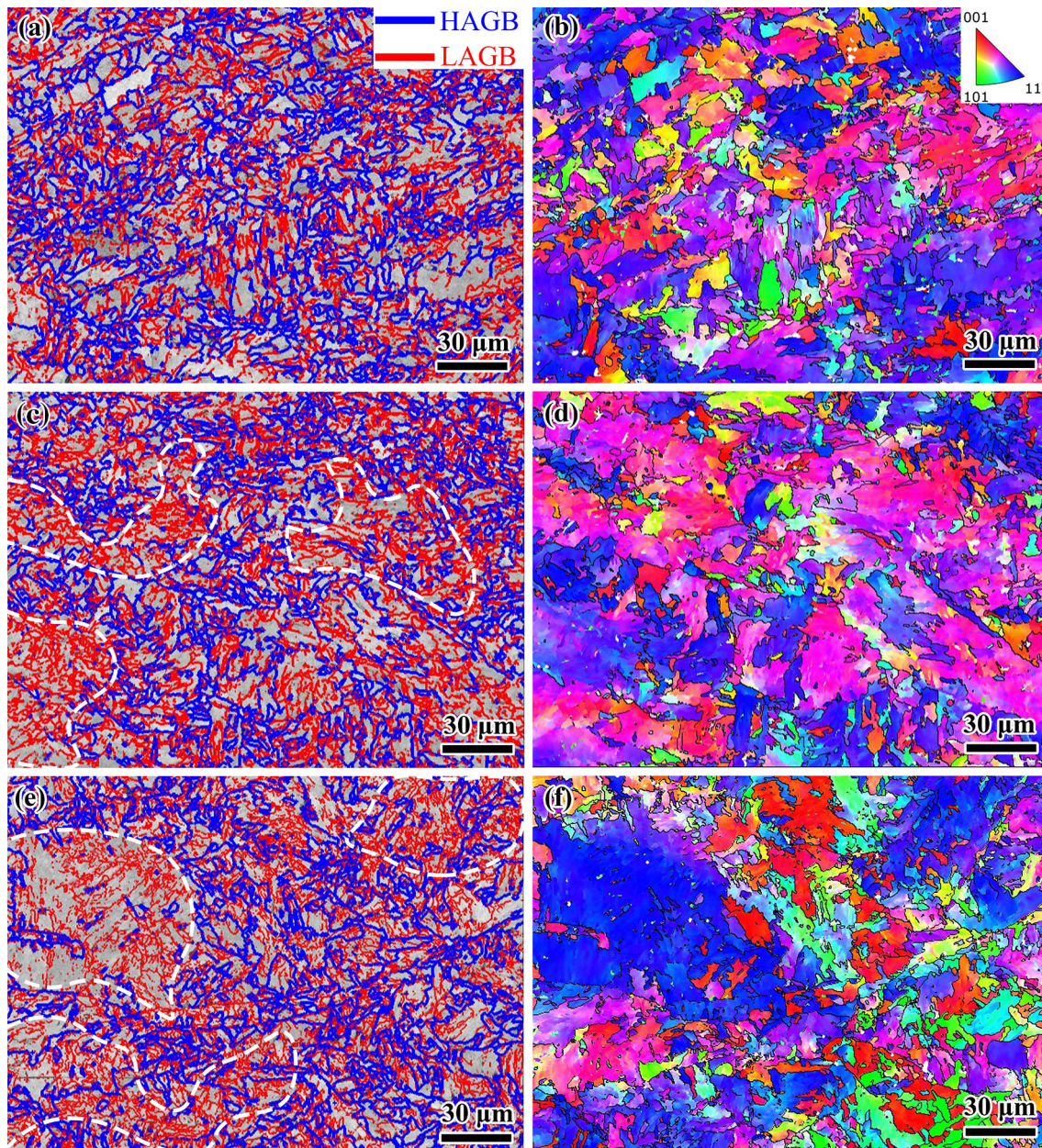


Fig. 5 Grain boundary misorientation distribution and IPF maps of S1–S3 steels at 1/2 thickness. **a, b** S1 steel; **c, d** S2 steel; **e, f** S3 steel

steel exhibits no plastic deformation, and only secondary cracks are presented, even under the large-angle deformation zone, as shown in Fig. 11f, g. The occurrence of plastic deformation and secondary cracks necessitates more energy expenditure, which is conducive to the improvement of impact toughness and resistance to fracture under extreme conditions.

3.2.3 Delamination characteristics

As depicted in Fig. 12, delaminated cracks of varying magnitudes are witnessed on the surface of the impact

fracture at different temperatures and the delamination is perpendicular to the fracture surface. S2 and S3 steels delamination commences to make an appearance at $-20\text{ }^{\circ}\text{C}$, while S1 steel commences to reveal prominent delamination at lower temperatures ($-60\text{ }^{\circ}\text{C}$). Further, as the impact temperature decreases, a noticeable increasing tendency can be observed in the length of the delaminated crack on the surface, while its width exhibits a parabolic trend, initially increasing before tapering off as exhibited in Fig. 12. Moreover, the delamination itself exhibits brittle fracture characteristics, as illustrated in Fig. 12j–l. With S3 steel as the representative sample, the propagation depth of

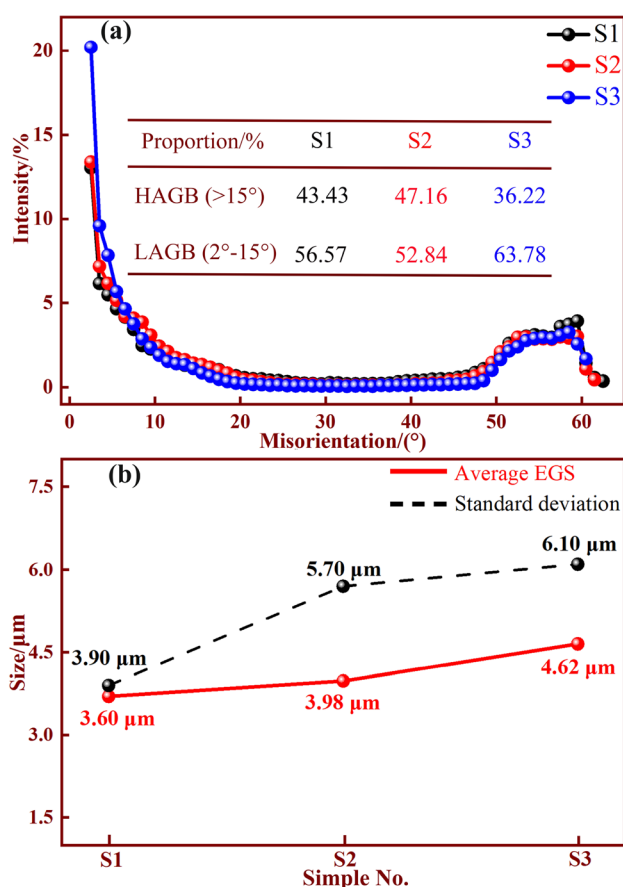


Fig. 6 Frequency of grain boundaries with different misorientation angles (a) and average EGS and its standard deviation (b)

the delaminated cracks was further analyzed to reveal the interaction between delamination and low-temperature toughness, as depicted in Fig. 13. Clearly, the depth of the delaminated crack experiences a gradual amplification with the decrease in temperature. In addition, an obvious plastic deformation zone was observed near the delaminated crack (Fig. 13e), which is the direct evidence of delamination toughening.

4 Discussion

4.1 Microstructural evolution

The microstructure is intricately linked to chemical compositions and hot rolling processes. In the present work, different microstructures (like phase content, grain boundary distribution and grain size) in S1–S3 steels were obtained by composition regulation under the same process, as illustrated in Sect. 3.1. The reasons for microstructural evolution are discussed in detail in the following paragraphs.

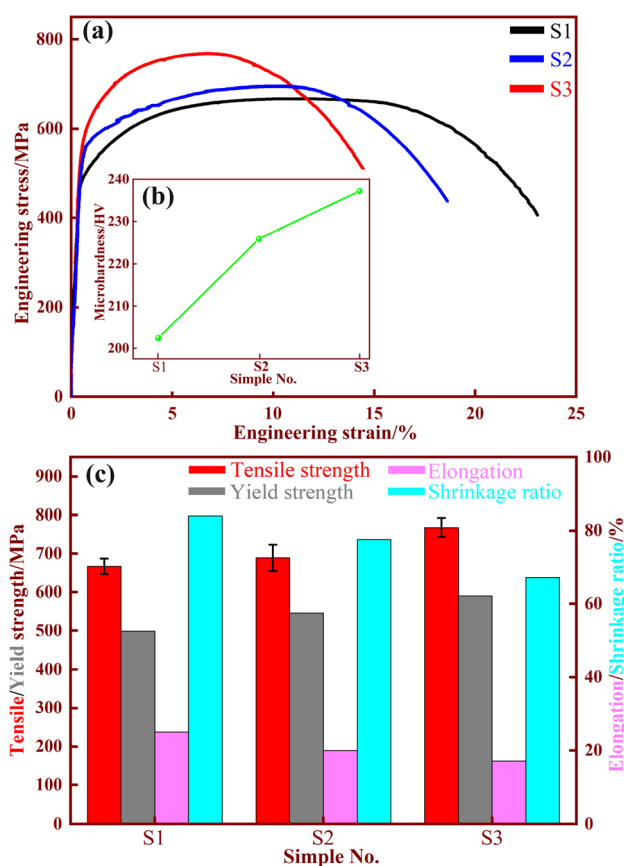


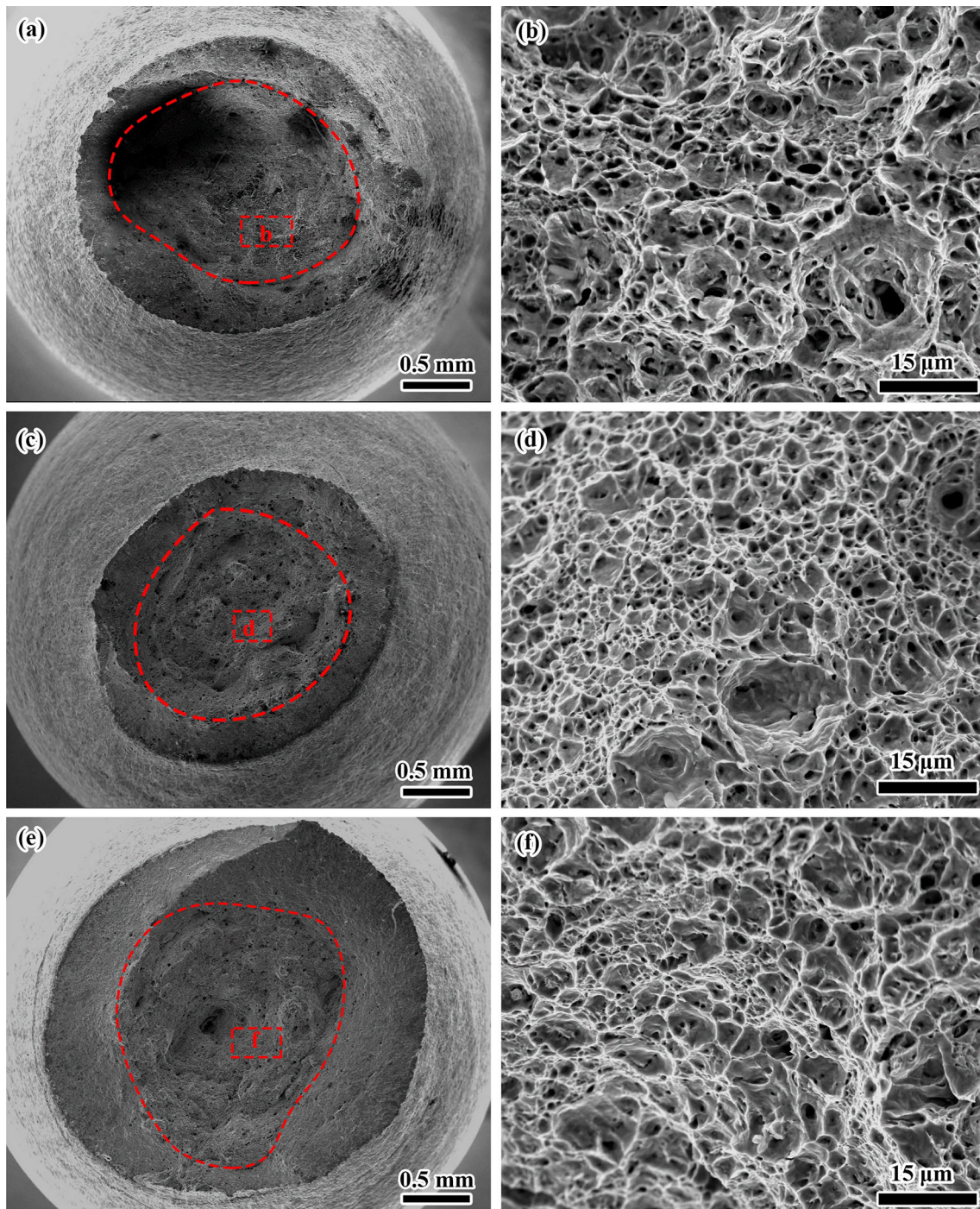
Fig. 7 Engineering stress–strain curves (a), Vickers microhardness (b) and tensile strength, yield strength, elongation and surface shrinkage (c) of S1–S3 steels at 1/2 thickness

As the element of stable austenite, Ni can expand the austenite phase region and significantly decrease the transformation temperature of austenite into ferrite [28, 29]. Lowering the temperature at which ferrite transitions leads to the narrowing of its growth interval, which limits the growth of grains. Therefore, the increase in Ni content can effectively refine the grains, that is, the grains of S1 steel are finer (EGS is 3.60 μm). Concurrently, as a solid solution element, Ni can effectively inhibit the diffusion rate of the C element, increasing the activation energy for diffusion [7]. Therefore, Ni can suppress diffusive transformation. As the bainitic transformation is through a semi-diffusionless mechanism, increasing the Ni content results in higher bainite content in S1 steel under the same TMCP process. Additionally, bainite lath/sub-grain boundaries are commonly LAGBs [30], which results in HAGBs being slightly lower in S1 steel compared to S2 steel.

Several studies indicate that the molybdenum element can shift the continuous cooling transition (CCT) curve to the right, and delay/suppress ferrite formation while promoting or extending bainite formation field [31, 32].

Table 3 Room temperature tensile property of S1–S3 steels

Sample	Tensile strength/MPa	Yield strength/MPa	Total elongation/%	Yield ratio	Section shrinkage/%	Vickers microhardness/HV
S1	667	498	25	0.74	84.0	201.40
S2	689	543	20	0.78	77.5	225.50
S3	768	590	17	0.77	67.2	237.15

**Fig. 8** Morphologies of tensile fractures at 1/2 thickness of S1–S3 steels. a, b S1 steel; c, d S2 steel; e, f S3 steel

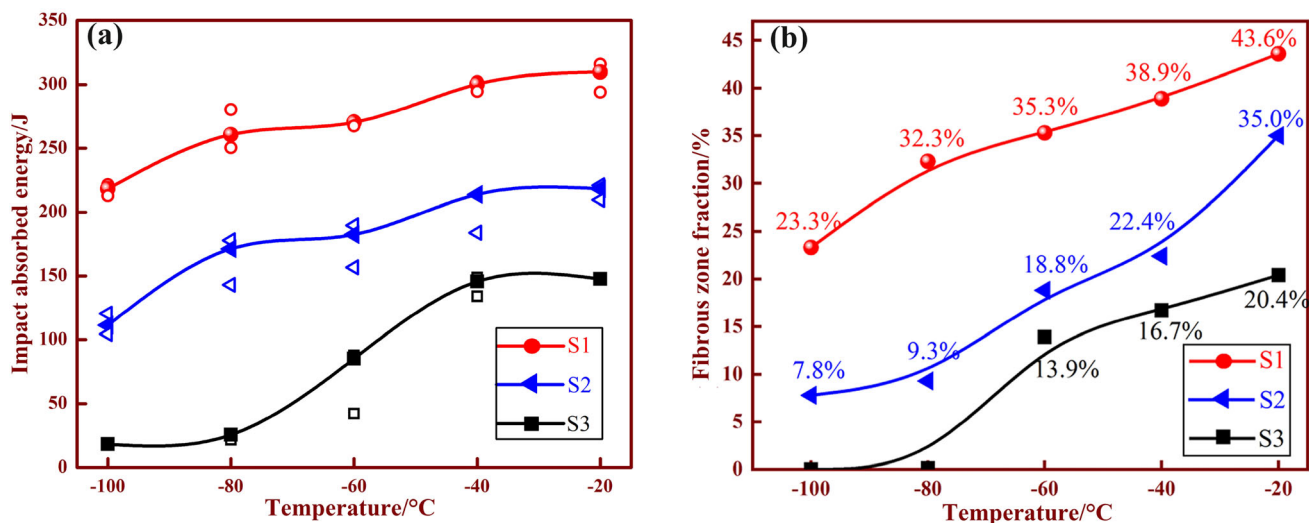


Fig. 9 Impact energy (a) and fiber area ratio at fracture surface (b) of S1–S3 steels at different temperatures

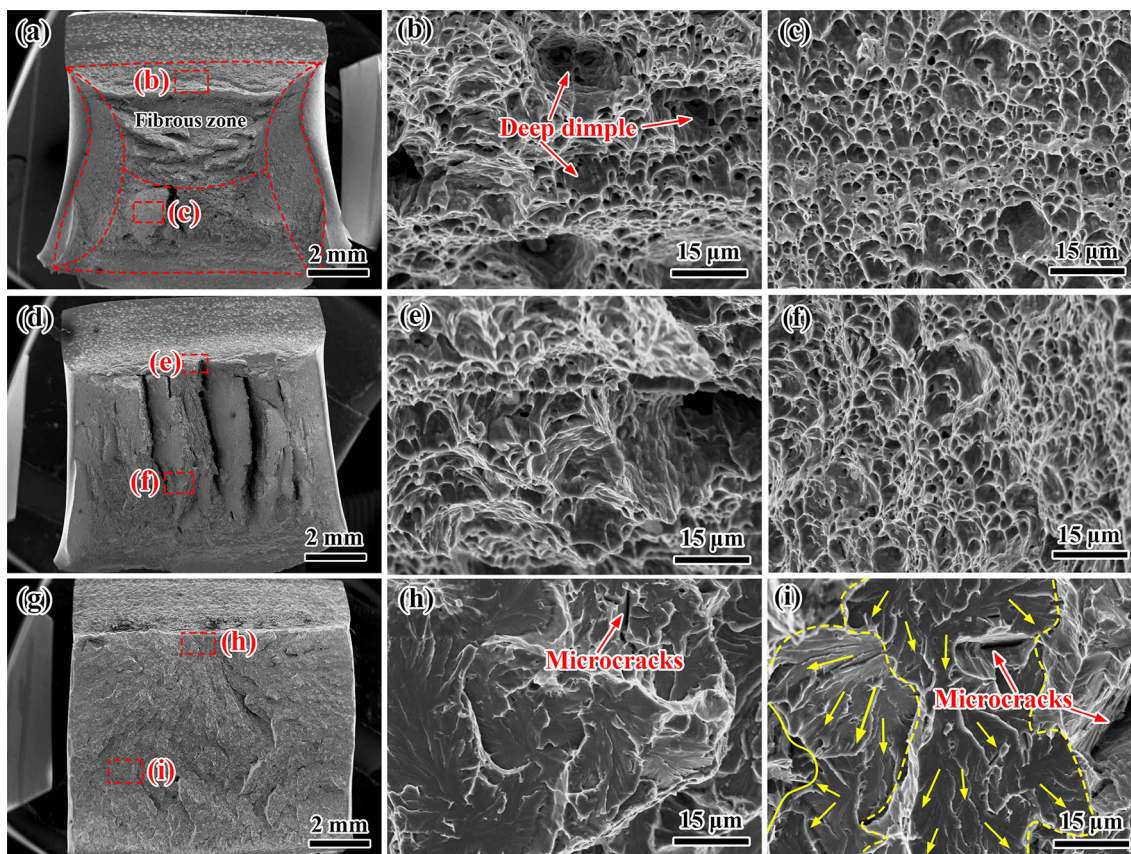


Fig. 10 Microscopic impact fractographs of S1–S3 steels at $-100\text{ }^{\circ}\text{C}$. a–c S1 steel; d–f S2 steel; g–i S3 steel

Therefore, more under-cooled austenite can transform into bainite in Mo-containing steel under the same TMCP process. This is the fundamental reason for the formation of full GB microstructure in S3 steel, as shown in Fig. 2e, f. This indicates that Mo promotes the formation of GB, which is consistent with the result of Chen et al. [33] and

Tian et al. [14]. Bainite usually has a high dislocation density, which is easy to cause dislocation entanglement and dislocation motion disorder. This property is conducive to improving the strength of steel [34]. In addition, GB is usually composed of bainitic ferrite (BF) and M–A constituents dispersed in the BF matrix [35]. Thus, S3 steel

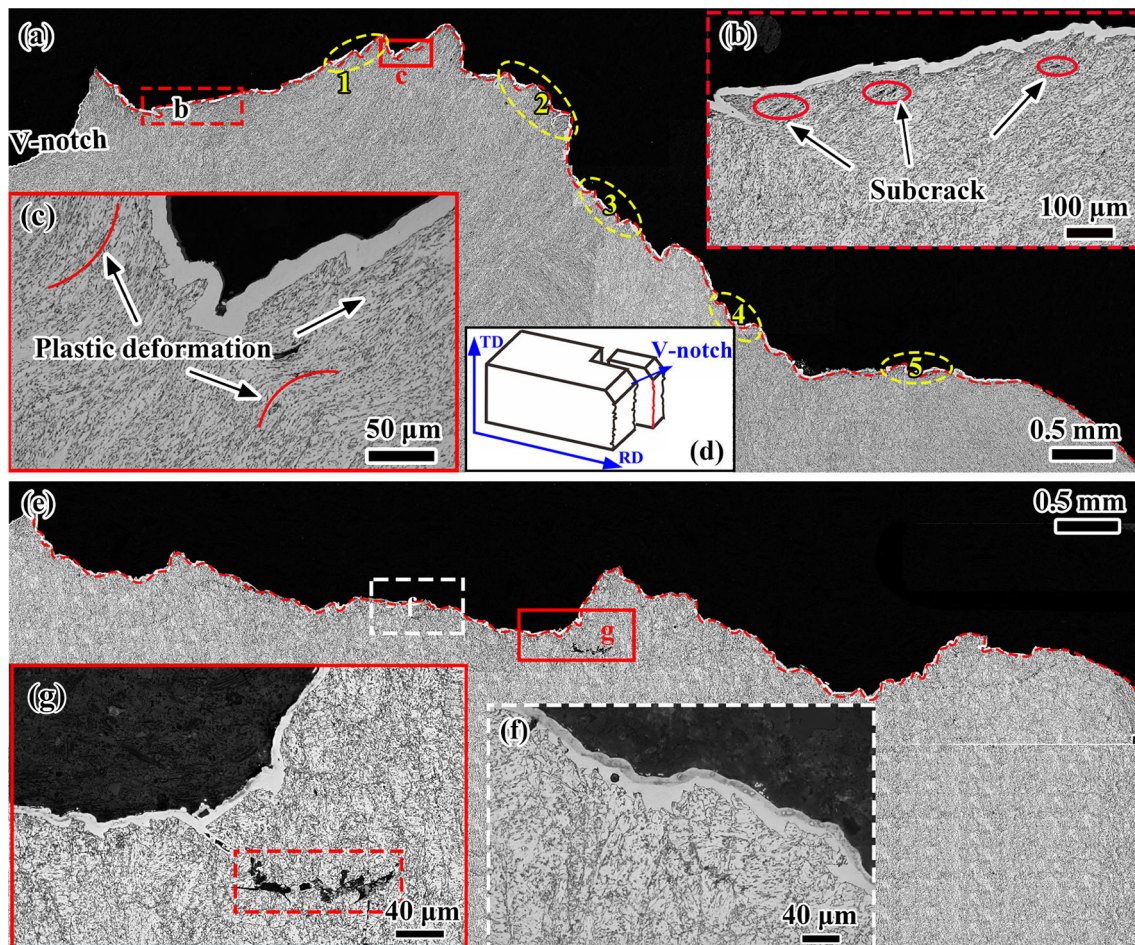


Fig. 11 Morphology along cross-section near impact fracture tested at $-100\text{ }^{\circ}\text{C}$. **a** S1 steel; **e** S3 steel; **d** observation locations near V-notch; **b**, **c**, **f**, **g** magnified morphology corresponding to local region

contains a greater quantity of M–A islands (Fig. 3e, f) that are relatively hard and further increase the strength of S3 steel. In addition, HAGBs are mostly found between the battens of different bain groups. It can be seen from EBSD (Fig. 5d) that GB presents the same or similar color, indicating that their misorientation is small. Therefore, the high content of bainite causes an increase in the proportion of LAGBs in S3 steel, as depicted in Fig. 5e. In addition, Fig. 4 reveals that the addition of Mo promotes the precipitation of carbides and refines their size. This is mainly because Mo can reduce the diffusion coefficient of other precipitated elements, retard the precipitation time, and refine the precipitates [36]. There is also evidence to suggest that the addition of Mo helps reduce the interfacial energy between the precipitated phase and the matrix, thereby increasing the density of the precipitates. Additionally, carbides generally preferentially nucleate at dislocations [37], and GB usually has high-density dislocation. Therefore, there are more abundant carbide nucleation sites in S3 steel, which further promotes the formation of carbides. These nano-size precipitates can

hinder the dislocation sliding and result in a desired precipitation-strengthening effect by pinning effect. Therefore, the bainitic transformation, dislocation strengthening and precipitation strengthening can explain the improvement in the tensile strength of the S3 steel.

Based on all the above results, we find that it is feasible to adjust the microstructure of the steel by controlling the alloying component. Adding a proper amount of Ni is helpful to refine grain and adjust phase content. The promotion function of Mo on bainite transformation is a complex process. Mo elements played a role in regulate the morphology of precipitates.

4.2 Relationship between microstructure and low-temperature toughness

As is well-known, as a rigid second phase, the M–A island is crucial to the toughness of steel. Generally, the critical fracture stress can be calculated as follows classical Griffith theory [38]:

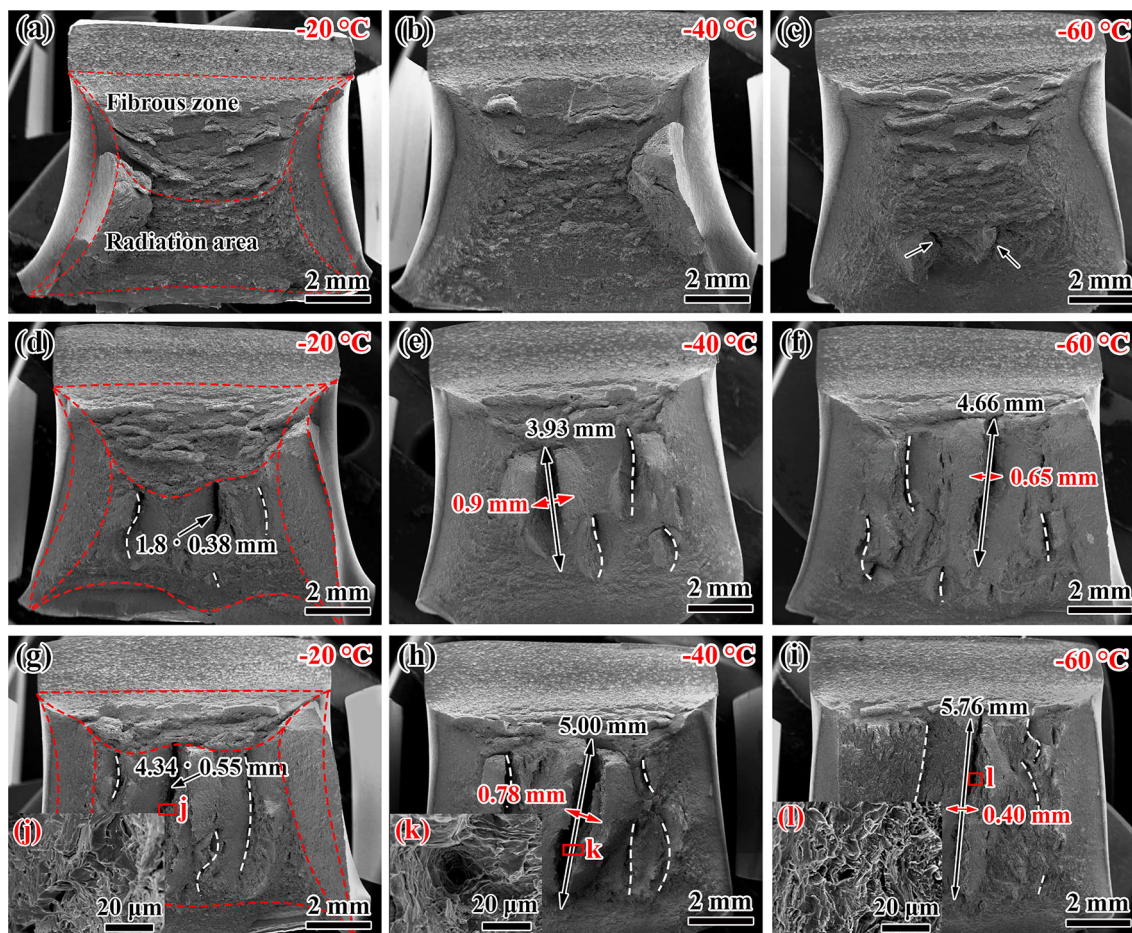


Fig. 12 Macroscopic impact fracture morphologies and delaminated cracks characteristic of S1–S3 steels at different temperatures. **a–c** S1 steel; **d–f** S2 steel; **g–i** S3 steel; **j–l** fracture morphology corresponding to local region

$$\sigma_{c'} = \left(\frac{\pi E \gamma'}{(1 - \nu^2) d_0} \right)^{1/2} \quad (4)$$

where γ' is the effective surface energy; ν is the Poisson's ratio; d_0 is micro-crack size; and E is the Young's modulus. Here, the maximum width of M–A island can be referred to as d_0 [5]. Equation (4) indicates that diminishing the diameter of M–A islands could increase the critical fracture stress, consequently augmenting the challenge of fracture propagation and improving low-temperature toughness. To further verify the above conclusion, the microstructure of S1 and S3 steels near the impact primary crack was further analyzed by SEM, as depicted in Fig. 14. Clearly, the primary crack changes the direction once it encounters the small-size and uniformly dispersed M–A islands. This phenomenon is more prominent in S1 steel as indicated by the yellow arrows in Fig. 14a. On the contrary, the primary crack passes straightly through the large-size M–A islands; moreover, micro-voids also tend to arise in larger or closely connected M–A islands, as shown in Fig. 14b. This indicates that stress concentration is more likely to occur at

large-size M–A islands, which assists cleavage fracture [39]. The effect of M–A islands on crack propagation can further understand through the model of crack propagation in Fig. 14c, d. M–A island size around the crack was further calculated, and the results showed that small-size ($\leq 2.2 \mu\text{m}$) and uniformly dispersed M–A islands have a powerful retarding effect on crack propagation and create a more tortuous propagation path, which will consume more energy and promote toughness. For comparison, these large-size ($> 2.2 \mu\text{m}$) M–A islands do not impede the crack propagation, but become the main locations of crack germination. These results are consistent with several research groups. As demonstrated by Li et al. [40], the coarse M–A island along the grain boundary is the main factor promoting brittle fracture, while the smaller M–A island is favorable in obtaining high toughness. Li et al. [24] also found a comparable toughness enhancement phenomenon in the presence of minuscule M–A islands.

Moreover, the content of M–A islands also has a significant effect on the low-temperature toughness. In our present study, the low-temperature toughness (LT) is

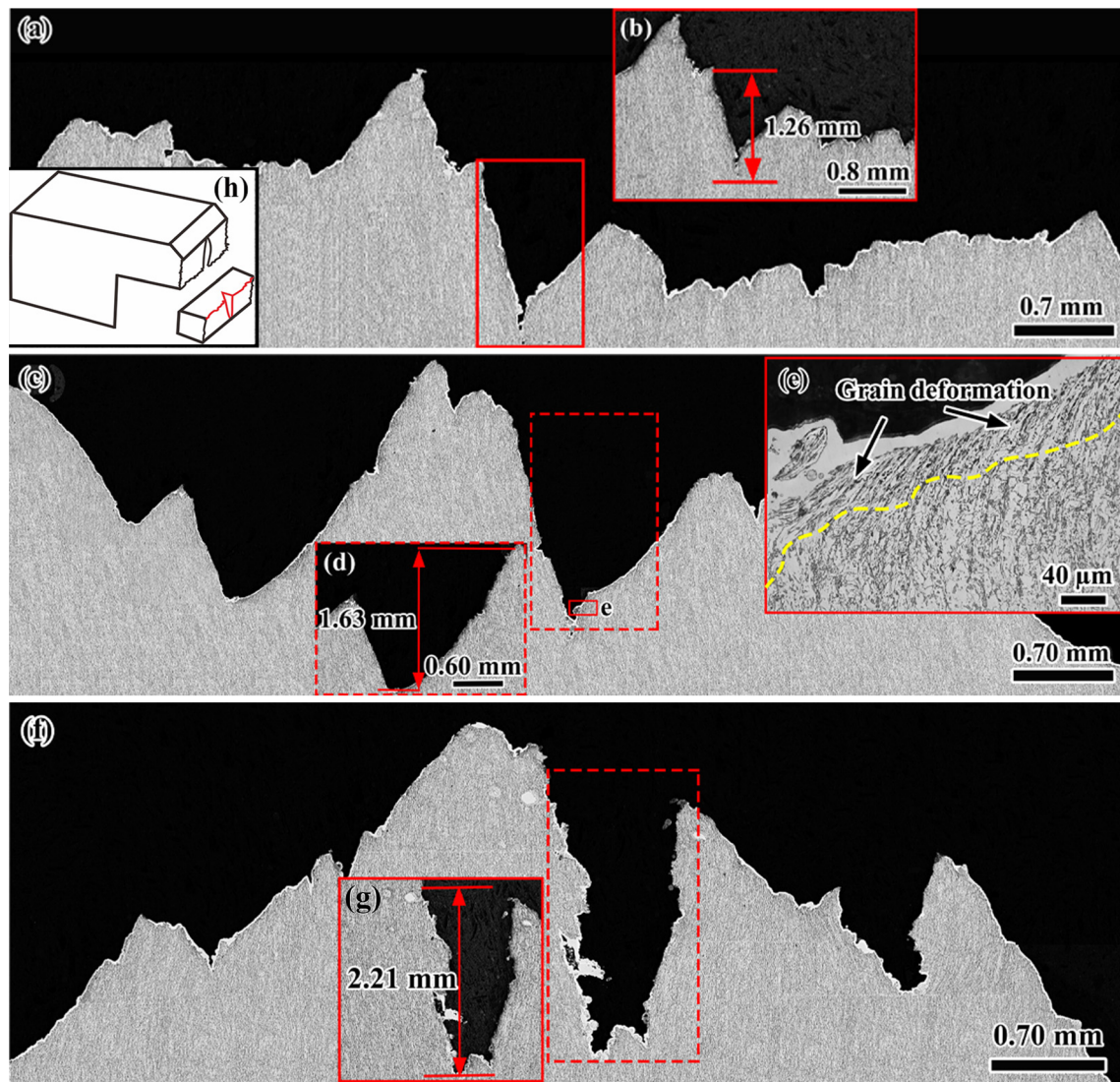


Fig. 13 Depth of delaminated crack at different temperatures of S3 steel. **a** $-20\text{ }^{\circ}\text{C}$; **c** $-40\text{ }^{\circ}\text{C}$; **f** $-60\text{ }^{\circ}\text{C}$; **h** observation locations near V-notch; **b**, **d**, **e**, **g** magnified morphology corresponding to local region

negatively influenced by the increase in M–A islands content (MC) (i.e., $LT_{S1} > LT_{S2} > LT_{S3}$; $MC_{S1} < MC_{S2} < MC_{S3}$), indicating that an overabundance of M–A islands can intensify fracture and weaken the toughness. It has also been reported that M–A islands at grain boundaries are more sensitive to fracture and stringer M–A islands are easier to detach from the matrix [21]. Through comprehensive analysis of M–A islands parameter, low content (2.21%) and small size (1.76 μm) of M–A islands are the key to promote the excellent low-temperature toughness of S1 steel. On the contrary, the large size (2.8 μm) and high content (3.84%) of M–A islands deteriorate the low-temperature toughness of S3 steel.

Generally, in the process of crack propagation, the deflection effect occurs when the crack encounters

HAGBs, which blunt crack tips and delayed fracture. However, not only LAGBs has no hindrance to crack propagation, but their aggregation distribution is more likely to cause stress concentration and cause fracture [41, 42]. Therefore, the high density and uniform distribution of HAGBs in S1 steel are an effective barrier to crack propagation, which further improves the toughness of S1 steel. In addition, the ductile–brittle transition temperature (DBTT) of steel can be determined by Eq. (5) [43]:

$$\text{DBTT} = T_t - Kd^{-1/2} \quad (5)$$

where T_t is a variable that depends on tensile properties; d is EGS; and K is constant. Therefore, EGS refinement has an obvious effect on DBTT reduction. Therefore, the higher density of HAGBs (43.43%) and fine average EGS

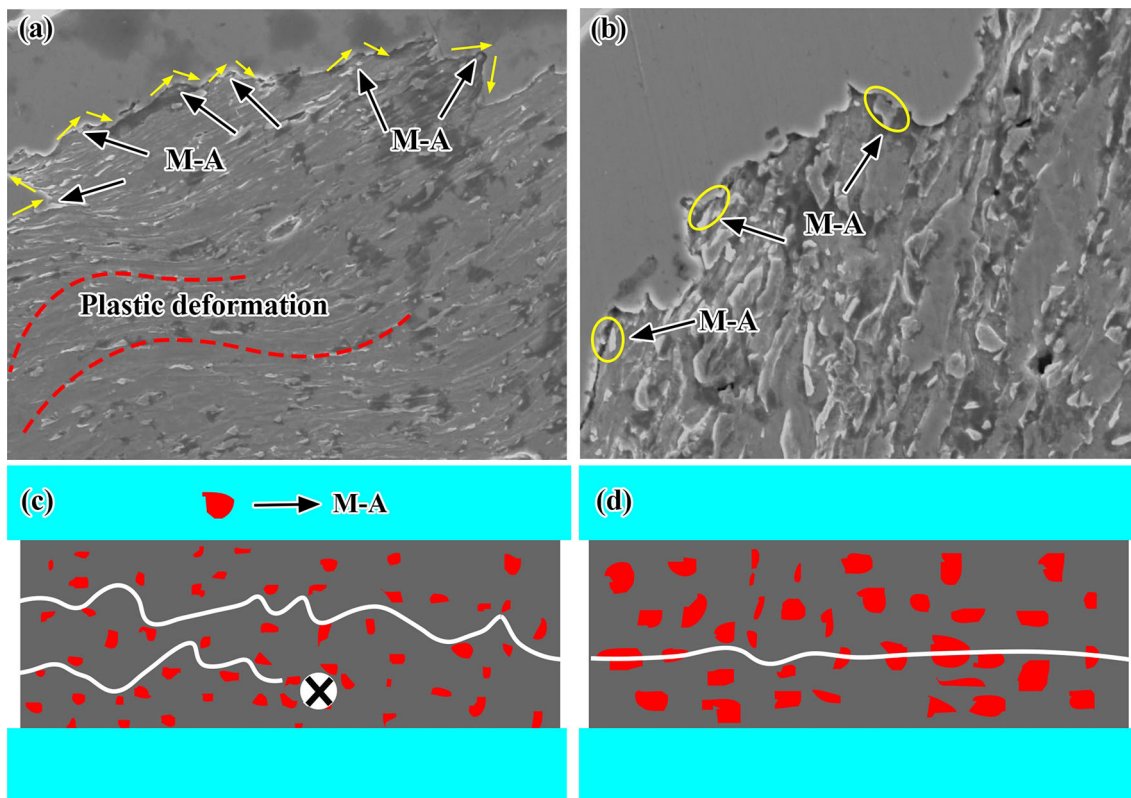


Fig. 14 Effect of M–A islands morphology on crack propagation in S1 and S3 steels (a, b) and model of crack propagation at M–A islands (c, d)

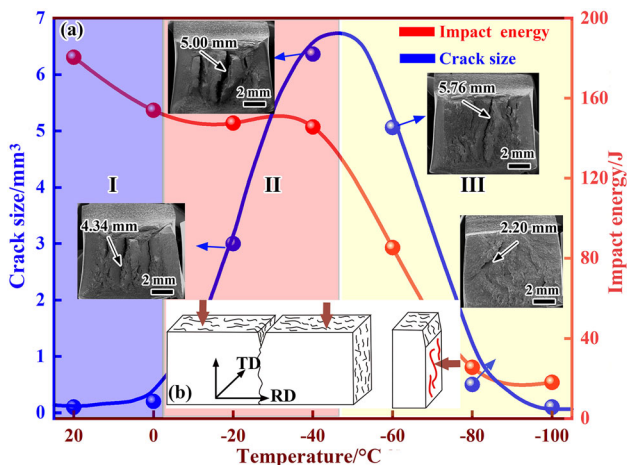


Fig. 15 Relationship between delamination and impact toughness at different temperatures (a) and transverse delamination mechanism (b)

(3.6 μm) in S1 steel are another reason for its excellent low-temperature toughness. In conclusion, besides the effect resulting from M–A islands, EGS, grain boundary misorientation and so on have an important effect on low-temperature toughness. The key to achieve excellent low-temperature toughness lies in multidimensional microstructure optimization.

4.3 Delamination toughening mechanism

Generally, delamination is a common phenomenon for the fracture surface of hot-rolled steel, which is usually related to microcrack, weak interface, and texture, etc. [44, 45]. This delamination phenomenon can be found in some reports. For instance, Cao et al. [46] reported that delamination makes the ferrite/martensite steel obtain high-impact energy. Yang et al. [47] demonstrated that the absorption of energy by delamination during the fracture process engenders additional plasticity and increases the impact energy. These studies evinced that delamination is advantageous to the improvement of toughness.

In our present study, the delamination is parallel to the rolling surface (Fig. 15b), which is conducive to reducing the triaxial stress [44]. The deep groove shape delamination gives the main fracture a jagged appearance, which passivates the main fracture surface and expends energy, and contributes to the improvement of toughness, even though delamination itself is a brittle fracture. In addition, as an example, S3 steel is used to calculate the volume of delamination according to its length, width and depth at different temperatures (delamination of smaller size (< 0.10 mm) was ignored) to evaluate its contribution to toughness, as depicted in Fig. 15. The volume of delamination changes in a parabolic manner as temperature

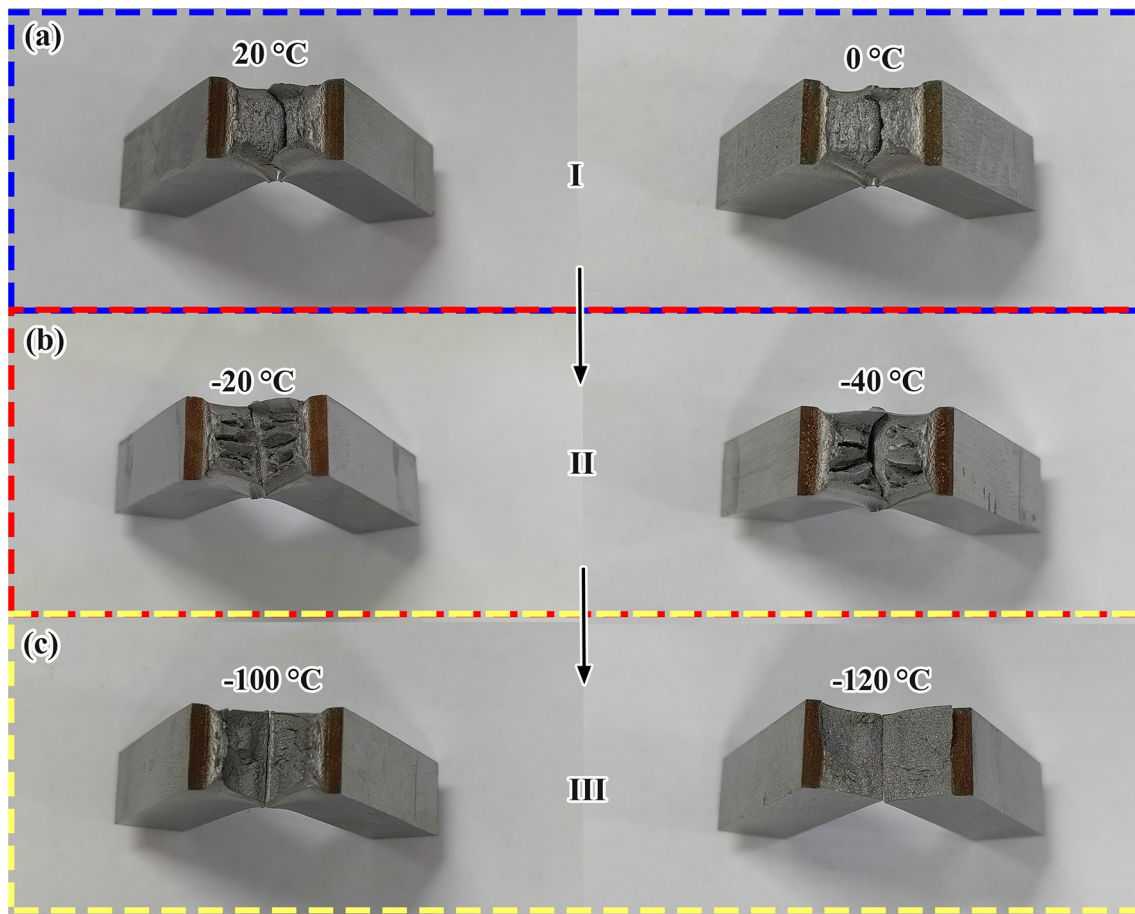


Fig. 16 Impact specimen fracture macroscopic topography at different temperatures

decreases, as shown in Fig. 15a, indicating that the enhancement of toughness by delamination exhibits a fluctuating characteristic. Delamination toughening can be described as progressing via three stages: delamination incubation stage (I), delamination expansion stage (II), and delamination degradation stage (III) (Fig. 15). When the impact temperature is high or impact energy is high, delamination does not form or form small-size delamination (stage I). At this stage, complete ductile fracture manifests in the sample, as exhibited in Fig. 16a. Delamination begins to appear and gradually strengthens with a further decrease in impact temperature (stage II). At this stage, the effect of delamination on toughness is progressively strengthened, which substantially retards the decrease rate of the impact energy, and effectively reduces the DBTT, as shown by the red line in Fig. 15. As the temperature continues to decrease, the brittleness of the sample increases (stage III). At this stage, the delamination toughening effect is gradually weakened, and the impact energy decreases sharply. The delamination will disappear when the sample is completely brittle fracture, as shown in Fig. 16c.

5 Conclusions

1. The addition of 2 wt.% Ni in S1 steel resulted in lower austenite to the ferrite transition temperature, which retards the growth of ferrite and refines grain size. Refined average effective grain size (3.60 μm), dense HAGBs and tiny M–A islands (1.76 μm) synergistically inhibit crack propagation. The optimized microstructure greatly reduces DBTT, and thus, S1 steel obtains the optimal impact toughness (Charpy impact energy of 218.2 J at $-100\text{ }^\circ\text{C}$).
2. Addition of Mo promotes the formation of granular bainite during TMCP. By adding 0.2 wt.% Mo, the average EGS coarsened from 3.98 to 4.62 μm , HAGBs content decreased to 36.22%, and the average size of M–A islands increased from 1.88 to 2.80 μm . In addition, the addition of Mo is beneficial to the refinement and precipitation of carbides. With these changes, the tensile strength is increased while the low-temperature toughness greatly deteriorates.
3. During the fracture process, delamination plays a critical role in improving the impact toughness due to

its effective dissipation of the energy, and impedes the decline of impact energy, reducing DBTT. Especially in the delamination expansion stage, the toughening effect is most prominent.

Acknowledgements This work is supported by the Project of Promoting Talents in Liaoning province (Grant No. XLYC2007036). The authors extend their gratitude to Dr. Y.H. Sun and Dr. N. Xiao (Analytical and Testing Center of Northeastern University, China) for the help with the LA-EBSD technique.

Declarations

Conflict of interest The authors have no known competing financial interests or personal relationships that could have appeared to influence the work reported in this paper.

References

- [1] Y. Zou, Y. Han, H.S. Liu, H.X. Teng, M.S. Qiu, F. Yang, *Mater. Charact.* 187 (2022) 111828.
- [2] C. Gao, M.Q. Yang, J.C. Pang, S.X. Li, M.D. Zou, X.W. Li, Z.F. Zhang, *Mater. Sci. Eng. A* 832 (2022) 142418.
- [3] M. Frichtl, Y. Anwar, A. Strifas, S. Ankem, *Met. Mater. Int.* 29 (2023) 879–891.
- [4] Y. Zhang, S. Wang, G. Xu, G. Wang, M. Zhao, *Int. J. Fatigue* 163 (2022) 107027.
- [5] J. Zhao, W. Hu, X. Wang, J. Kang, G. Yuan, H. Di, R.D.K. Misra, *Mater. Sci. Eng. A* 666 (2016) 214–224.
- [6] X. Qi, P. Huan, X. Wang, X. Shen, Z. Liu, H. Di, *Mater. Sci. Eng. A* 851 (2022) 143656.
- [7] A.R. Hosseini Far, S.H. Mousavi Anijdan, S.M. Abbasi, *Mater. Sci. Eng. A* 746 (2019) 384–393.
- [8] H.F. Lan, L.X. Du, R.D.K. Misra, *Mater. Sci. Eng. A* 611 (2014) 194–200.
- [9] N. Zhou, R. Song, R. Song, X. Li, J. Li, *Steel Res. Int.* 89 (2018) 1700552.
- [10] J. Hu, L.X. Du, Y. Dong, Q.W. Meng, R. Misra, *Mater. Charact.* 152 (2019) 21–35.
- [11] J. Kong, L. Zhen, B. Guo, P. Li, A. Wang, C. Xie, *Mater. Des.* 25 (2004) 723–728.
- [12] W. Fu, C. Li, X. Di, K. Fu, H. Gao, C. Fang, S. Lou, D. Wang, *Mater. Sci. Eng. A* 849 (2022) 143469.
- [13] Y. Sun, S. Hu, Z. Xiao, S. You, J. Zhao, Y. Lv, *Mater. Des.* 41 (2012) 37–42.
- [14] Y. Tian, J. Zhou, Y. Shen, Z. Qu, W. Xue, Z. Wang, *Adv. Eng. Mater.* 22 (2020) 1901553.
- [15] Y. Lu, X.D. Liu, Y. Li, J.F. Li, D. Wu, K. Lv, *Foundry Technol.* 27 (2006) 1342–1345.
- [16] Q. Wu, S. He, P. Hu, Y. Liu, Z. Zhang, C. Fan, R. Fan, N. Zhong, *Mater. Sci. Eng. A* 862 (2023) 144496.
- [17] L.P. Karjalainen, T.M. Maccagno, J.J. Jonas, *ISIJ Int.* 35 (1995) 1523–1531.
- [18] F.S. LePera, *Metallography* 12 (1979) 263–268.
- [19] N. Huda, A.R.H. Midawi, J. Gianetto, R. Lazor, A.P. Gerlich, *Mater. Sci. Eng. A* 662 (2016) 481–491.
- [20] S. Moenifar, A.H. Kokabi, H.R.M. Hosseini, *Mater. Des.* 32 (2011) 869–876.
- [21] K.I. Sugimoto, N. Usui, M. Kobayashi, S.I. Hashimoto, *ISIJ Int.* 32 (1992) 1311–1318.
- [22] Y. Tian, H.T. Wang, Q.B. Ye, Q.H. Wang, Z.D. Wang, G.D. Wang, *Mater. Sci. Eng. A* 794 (2020) 139640.
- [23] B. Wang, Q.Q. Duan, P. Zhang, Z.J. Zhang, X.W. Li, Z.F. Zhang, *Mater. Sci. Eng. A* 771 (2020) 138553.
- [24] H.F. Li, S.G. Wang, P. Zhang, R.T. Qu, Z.F. Zhang, *Mater. Sci. Eng. A* 729 (2018) 130–140.
- [25] X.J. Shen, D.Z. Li, S. Tang, J. Chen, H. Fang, G.D. Wang, *Mater. Sci. Eng.* 766 (2019) 138342.
- [26] H. Luo, X. Wang, Z. Liu, Z. Yang, *J. Mater. Sci. Technol.* 51 (2020) 130–136.
- [27] K. Srinivasan, Y. Huang, O. Kolednik, T. Siegmund, *J. Mech. Phys. Solids* 56 (2008) 2707–2726.
- [28] Z.B. Jiao, J.H. Luan, Z.W. Zhang, M.K. Miller, W.B. Ma, C.T. Liu, *Acta Mater.* 61 (2013) 5996–6005.
- [29] V.R. Mattes, *Microstructure and mechanical properties of HSLA-100 steel*, Naval Postgraduate School, Monterey, USA, 1990.
- [30] S.Y. Shin, B. Hwang, S. Lee, K.B. Kang, *Metall. Mater. Trans. A* 38 (2007) 537–551.
- [31] Z. Tang, W. Stumpf, *Mater. Charact.* 59 (2008) 717–728.
- [32] H. Hu, G. Xu, L. Wang, Z. Xue, Y. Zhang, G. Liu, *Mater. Des.* 84 (2015) 95–99.
- [33] X.W. Chen, G.Y. Qiao, X.L. Han, X. Wang, F.R. Xiao, B. Liao, *Mater. Des.* 53 (2014) 888–901.
- [34] X. Zhang, S. Liu, K. Wang, L. Yan, J. Wang, Q. Xia, H. Yu, *Mater. Sci. Eng. A* 884 (2023) 145578.
- [35] Y. Zhou, T. Jia, X. Zhang, Z. Liu, R.D.K. Misra, *Mater. Sci. Eng. A* 626 (2015) 352–361.
- [36] S.S. Xu, Y.W. Liu, Y. Zhang, J.H. Luan, J.P. Li, L.X. Sun, Z.B. Jiao, Z.W. Zhang, C.T. Liu, *Mater. Res. Lett.* 8 (2020) 187–194.
- [37] J. Hu, X. Li, Q. Meng, L. Wang, Y. Li, W. Xu, *Mater. Sci. Eng. A* 855 (2022) 143904.
- [38] D.A. Curry, J.F. Knott, *Met. Sci.* 13 (1979) 341–345.
- [39] B. Fang, H.S. Ding, L.G. Tong, L.Q. Pan, *Prog. Nat. Sci. Mater. Int.* 30 (2020) 110–117.
- [40] X. Li, X. Ma, S.V. Subramanian, C. Shang, R.D.K. Misra, *Mater. Sci. Eng. A* 616 (2014) 141–147.
- [41] G. Mao, C. Cayron, R. Cao, R. Logé, J. Chen, *Mater. Charact.* 145 (2018) 516–526.
- [42] X. Xu, Y. Tian, Q. Ye, R.D.K. Misra, Z. Wang, *Steel Res. Int.* 92 (2021) 2100274.
- [43] M. Dáz-Fuentes, Iza-Mendia, A.I. Gutiérrez, *Metall. Mater. Trans. A* 34 (2003) 2505–2516.
- [44] T. Inoue, F. Yin, Y. Kimura, K. Tsuzaki, S. Ochiai, *Metall. Mater. Trans. A* 41 (2010) 341–355.
- [45] M.E. Alam, S. Pal, S.A. Maloy, G.R. Odette, *Acta Mater.* 136 (2017) 61–73.
- [46] W. Cao, M. Zhang, C. Huang, S. Xiao, H. Dong, Y. Weng, *Sci. Rep.* 7 (2017) 41459.
- [47] X.L. Yang, Y.B. Xu, X.D. Tan, D. Wu, *Mater. Sci. Eng. A* 607 (2014) 53–62.

Springer Nature or its licensor (e.g. a society or other partner) holds exclusive rights to this article under a publishing agreement with the author(s) or other rightsholder(s); author self-archiving of the accepted manuscript version of this article is solely governed by the terms of such publishing agreement and applicable law.